An atomistic structural description of the ferrielectric polar phase involving non-coplanar cation displacements

T. Pramanik [a], Cho Sandar Htet [a], Alicia Manjón-Sanz [b,*], J. Liu [b], S. Ullah [a], J. Kong [a], C. Babori [c,d], A. Brézard-Oudot [c], L. Daniel [c,d], S.T. Misture [e], A. Pramanick [a,1,*]

[a] Department of Materials Science and Engineering, City University of Hong Kong, Hong Kong, PR China
[b] Neutrons Scattering Division, Oak Ridge National Laboratory, Oak Ridge, TN 37831, USA
[c] Group of Electrical and Electronic Engineers, Paris, University Paris-Saclay, Gif-sur-Yvette, France
[d] Sorbonne Université, CNRS, Laboratoire de Génie Electrique et Electronique de Paris, 75252 Paris, France
[e] Kazuo Inamori School of Engineering, Alfred University, Alfred, New York 14802, USA

ARTICLE INFO

ABSTRACT

Materials with antipolar-polar transformation are attractive for their large functional responses. However, the antipolar state remains controversial in many materials. For example, recent studies on archetypical antiferro-electric (AFE) materials indicate an incomplete compensation of antiparallel dipoles, which prompted their alternative definition as ferrielectric. Here, we investigated the origin of the ferrielectric (FIE) state in a classical AFE material using X-ray and neutron total scattering. We show that the FIE state arises from 3-dimensional modulation of the cation-centric electric dipoles, which can be viewed as periodic arrangement of 180° twin boundaries with non-Ising characteristics.

Materials that undergo antipolar to polar phase transitions exhibit large electric-field-induced changes in their surface charges and/or strain, which make them attractive for high/pulse power capacitors, high-strain electromechanical actuators and solid-state cooling applications [1-4]. Antiferroelectrics (AFE) are one class of archetypical antipolar materials. In the classical view, the electric dipoles in AFE are arranged in an antiparallel fashion within centrosymmetric unit cells [5], which leads to a net zero macroscopic polarization. However, under large applied electric-fields, the antiparallel dipoles can align parallel to each other, thereby constituting a transition to polar ferroelectric (FE) phase [6]. Upon removal of the electric-field, the dipoles revert back to their original antiparallel arrangement [7,8]. Although the classical model could phenomenologically describe the double polarization vs electric-field (P-E) hysteresis loop of AFEs [8,9], it has been challenged by recent observations of a non-zero remanent polarization in some well-know AFE materials, such as $PbZrO_3$ [10-13]. Instead, based on electron microscopy studies, it was proposed that many of the classical AFEs may indeed be ferrielectric, which implies that the antiparallel dipole moments do not exactly cancel each other [10,11,14,15]. Nevertheless, the atomistic model of an ferrielectric (FIE) state remains

unresolved. For example, it is unclear why the cation-centric dipoles should vary significantly across the different layers in a ferrielectric structure, given their similar chemical environments or what factors drive continuous rotation of polarization vector even in presence of strong dipole-dipole interactions.

To address these issues, herein, we investigated the structural state of a classic AFE $AgNbO_3$ (AGN), which is attractive for energy storage devices due to their characteristic double-loop polarization hysteresis and high breakdown strength [16-18]. Indeed, the exact polar state of AGN is controversial. In 1958, Francombe and Lewis reported a small remanent polarization for AGN at room temperature, which confounded them about whether to define AGN as ferroelectric or antiferroelectric [19]. Recently, other researchers also verified the existence of weak ferroelectricity in AGN [20-22]. However, the crystal structure of AGN is considered to have a centrosymmetric *Pbcm* space group, which precludes any spontaneous polarization [23-26]. Recently, Yashima et al., using a combination of convergent beam electron diffraction (CBED) and neutron powder diffraction (NPD), modeled the room temperature average phase (M1 structure) of AGN with orthorhombic polar *Pmc*2_1 space group [27], which was able to describe the weak polarization in
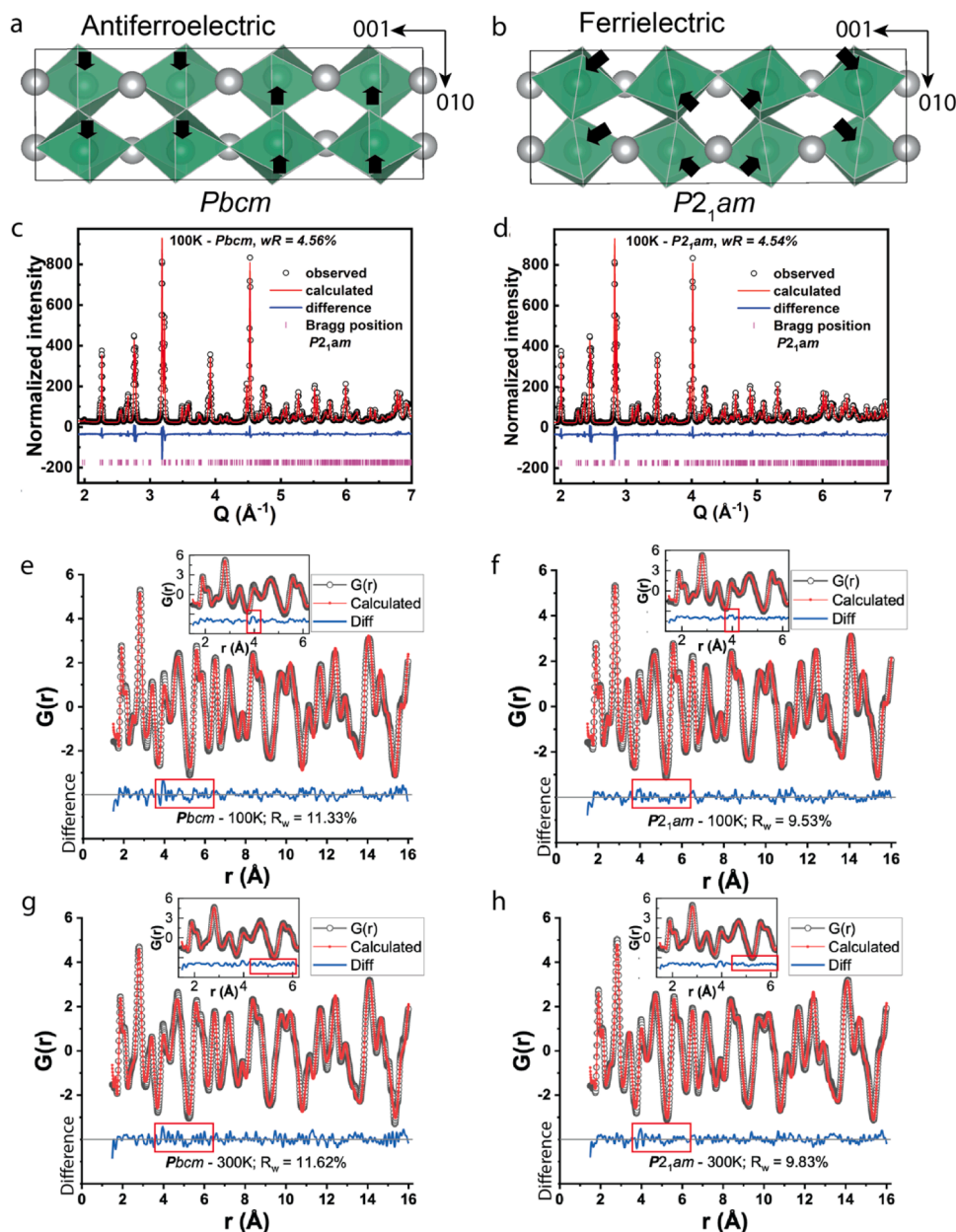
Fig. 1. (a,b) Illustration of the (a) antiferroelectric *Pbcm*, and (b) the ferrielectric *P2₁am* structures. (c,d) Rietveld refinement of the NPD data collected at 100 K using (c) *Pbcm* structural model and (d) *P2₁am* structural model. Observed (black symbols), calculated (red line), difference (blue line) profiles, and Bragg positions (red ticks) obtained after the Rietveld refinement using GSAS II software. Weighted residuals (Rw) are shown for both the refinements. Fits of neutron G(r) over the range 1.5 to 16 Å measured at 100 K and 300 K using *Pbcm* space group structure (**e** and **g**) and *P2₁am* space group structure (**f** and **h**). The difference between the measured and calculated data is shown by the blue curves at the bottom. The solid line represents the zero line for the difference plot. The PDF fit observed using the *P2₁am* model is better than the *Pbcm* model, which is reflected in the Rw values and also from the difference curves, such as highlighted by the red-colored boxes.

AGN based on antiparallel displacements of Ag^+, Nb^{5+}, and O^{2-} ions with unequal magnitudes. This was also verified by measurement of large remanent polarization [28] and non-linear optical properties at low temperatures [29], and later substantiated by Farid et al. [30].. Interestingly, Gao et al. proposed the existence of a ferrielectric polar symmetry (*Pmc2₁*) at the short-range (1.5 – 15 Å) and a centrosymmetric symmetry (*Pbcm*) at the long-range (15 – 40 Å) length scale [31,32], although the underlying structural rationale for ferrielectricity was not explained. It is noteworthy that local structural probes, such as nuclear magnetic resonance (NMR) [15] and Pair Distribution Function (PDF) [25,32], have indicated non-coplanar nature of cation displacements in archetypical AFEs, which is otherwise not detectable by neutron/X-ray diffraction or electron microscopy.

Herein, we revisit the structure of the FIE state in AGN by combining X-ray/neutron powder diffraction and neutron PDF. We show that both the non-coplanar nature as well as modulation of the neighboring electric dipoles in AGN ultimately derive from coupled Ag-O and Nb-O bonds, which are central to the evolution of its ferrielectric nature. We furthermore show that both of these aspects can be described based on a model of periodic twin boundaries, such as presented by us for the AFE structure of $NaNbO_3$ [33,34]. We also show for AGN, the periodic twin boundaries exhibit non-Ising characteristics, which allows for a more gradual transition of the neighboring dipole moments [35]. These findings enrich our understanding of the types of electric dipole configurations in dielectric materials and reveal the structural underpinnings of a FIE phase.
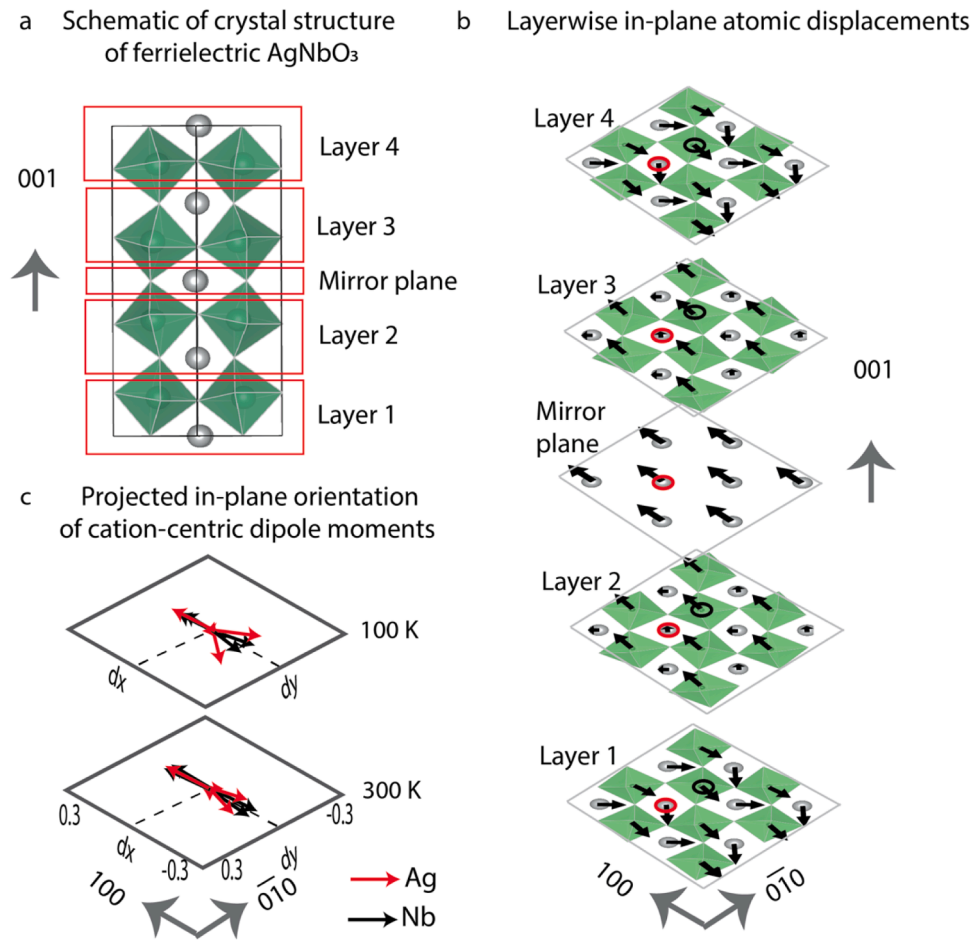
Fig. 2. **(a)** Schematic illustration of the ferrielectric crystal structure of $AgNbO_3$. The structure is segmented into different layers stacked along the 001 direction, in order to clarify the in-plane atomic displacements. (**b**) The layer-wise off-center cationic displacements at 100 K. The Nb atoms are placed within the oxygen octahdera marked in green (such as indicated by black circles) and the Ag atoms are marked in grey (such as indicated by red circles). The off-centred displacements of the Ag and Nb atoms are shown with black arrows. **(c)** The orientation of the projected cationic displacements on the a-b plane for 100 K and 300 K are shown. Note that the Ag and Nb cationic displacements in the a-b plane at 100 K have wider angular spread than the same at 300 K.

First, we undertook Rietveld analysis of powder X-ray (see SI [36]) and NPD data in order to determine whether the long-range structure belongs to an antipolar (*Pbcm*) (structural prototype shown in Fig. 1(a)) or polar (*P2$_1$am*) (structural prototype shown in Fig. 1(b)) space group. However, fitting of the 100 K and 300 K NPD data based on either of the structural models was equally satisfactory, as indicated by nearly equal weighted R_w factors (Fig 1(c) and 1 (d)) (300 K data for X-ray/neutron diffraction are shown in Figures S2, S3 in the SI [36]). It should be noted that the *P2$_1$am* space group is a subset of the *Pbcm* space group. Moreover, the unit cells of *P2$_1$am* and *Pbcm* space groups are equivalent with $a/b \approx 2^{(1/2)}$ a_p, $c \approx 4$ c_p, where a_p and c_p represent pseudocubic perovskite unit cell parameters. These factors limit the unequivocal determination of the average structure to be either antiferroelectric or ferrielectric. We also carried out two-phase Rietveld refinement, however the refinement resulted in negative U_{iso} and therefore not considered further. This led us to rule out any possibility of the coexistence of *P2$_1$am* and *Pbcm* phases at 300 K and 100K.

To resolve the structural ambiguity, we next analyzed neutron PDF data G(r) collected at 100 K and 300 K, which directly probes the local structural distortions in perovskite oxides [37-39]. See Supplementary Information for details of measurement of G(r)) [36]. The neutron bound coherent scattering lengths are: b_{Ag}~5.922 fm, b_{Nb}~7.054 fm and b_O~5.803 fm [40]. Since Ag and O scatter almost equally, while Nb scatters significantly more, neutron PDF provides very good sensitivity for all the corresponding atom-atom pair correlations. First, we

attempted fitting of the absolutely normalized G(r) using the antipolar *Pbcm* and polar *P2$_1$am* structural models, Figs. 1 (e- h). The fitting range of $r \sim 1.5$–16 Å is chosen to approximately correspond to the longest dimension of one unit cell and, therefore, represent the minimum length scale over which the symmetry elements could be applied and all possible nearest neighbor atom-atom connectivity examined. We observe that the experimental G(r) can be fitted better with the *P2$_1$am* structural model over that of *Pbcm*, which therefore clearly indicates that the structure of AGN is polar over short length scales ($r < 16$Å). Box-car type refinement indicated that the local polar *P2$_1$am* structure does not extend beyond 24 Å (see Supplementary Information [36] for details). In this respect, AGN is similar to other polar perovskites, where the bonding requirements of the cations (Ag^{+1} and Nb^{+5}) lowers the symmetry of the local structure vis-à-vis the long-range average structure [41].

To clarify the exact origin of net uncompensated polarization, we next examined the layer-wise atomic displacements. Fig. 2a depicts the definition of the different layers within the ferrielectric *P2$_1$am* structure of $AgNbO_3$. Note that in the current depiction, the Ag for layers 1 and 2 are located near the bottom of the oxygen octahedra (negative *c* axis direction), while the Ag for layers 3 and 4 are located near the top of the oxygen octahedra (positive *c* axis direction). The Ag displacements at the mirror plane ($z = 0.5$) are shown as a separate layer. Fig. 2b illustrates the vectorial representation of the layer-wise in-plane displacements of Ag and Nb within their respective oxygen environments at 100
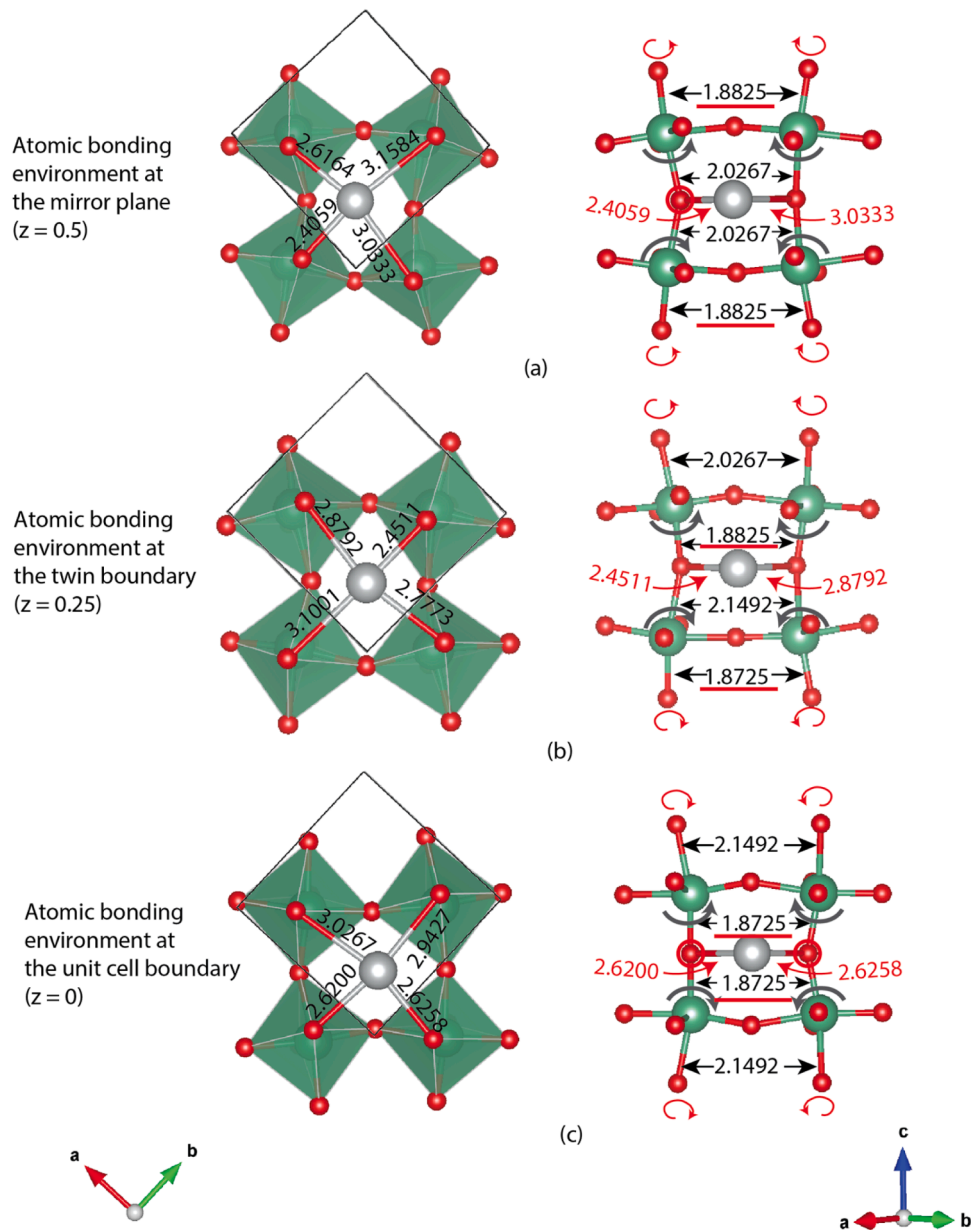
Fig. 3. Local bonding environment showing variations in cation-anion bond lengths for different layers of the $P2_1am$ structural model (units are in Å) at 100 K. The corresponding crystal orientations for the figures on the left and right panels are shown at the bottom, The shorter Nb-O bond lengths are underlined in red.

K. The orientation of the projected cationic displacements on the ab plane at 100 K and 300 K are shown in Fig. 2c. There are two aspects which are clearly evident: (a) the magnitude of the cation-centric dipoles is different for the different layers, with Ag-centric dipole moments having larger variation than the Nb centric dipoles, (b) the dipole moments for the different layers are misoriented with respect to each other. These two factors together lead to a net uncompensated polarization in ferrielectric AGN. Notably, the cationic displacements in Layers 1 and 4 approach parallel to <100> at 300 K, which can explain a experimentally observed reduction in remanent polarization with increasing temperature as the material approach an ideal AFE state [42]. Our results for cation-centric polarization components in AGN is consistent with earlier reports [15,32].

Below, we examine what casues the different magnitudes of layerwise cation-centric dipole moments . Fig. 3 shows the bonding environments for (a) $z = 0.5$, (b) $z = 0.25$ and (c) $z = 0$. Along the mirror plane ($z = 0.5$), the Ag atoms are bonded to the apical O of the neighboring Nb-O ocatehdra, and the shortest Ag-O bond length is ~ 2.41 Å In

comparison, for the Ag atoms near $z = 0.25$ and $z = 0$ (the unit cell boundary), the shortest Ag-O bond lengths are ~ 2.45 Å and ~2.62 Å, respectively. The different bonding environments for Ag can be explained due to coupled nature of the Ag-O and Nb-O bonds. The O $2p$ valence bands are known to overlap with the Nb $3d$ and Ag $4d$ states [43], leading to stronger bonding interactions and therefore formation of shorter Ag-O and Nb-O bonds. As shown in Fig. 3(a), the shorter Nb-O bonds are located away from the $z = 0.5$ plane, thereby leaving the apical O (marked in red circle) to interact more strongly with the neighboring Ag and form very short Ag-O bond (2.41 Å). In contrast, as shown in Fig. 3(c), the shorter Nb-O bonds are directed towards the $z = 0$ plane – this leaves the O $2p$ states (marked in red circle) to interact with the d orbitals of both the neighboring Nb and Ag. The later scenario weakens the Ag-O interaction and thereby increases the shortest Ag-O bond distance to 2.62 Å An intermediate situation exists for the Ag environment at $z = 0.25$, where the apical O atoms (marked with red circle) form short bonds with one of the Nb atoms and one Ag atom, which leads to an intermediate value of 2.45 Å for the shortest Ag-O
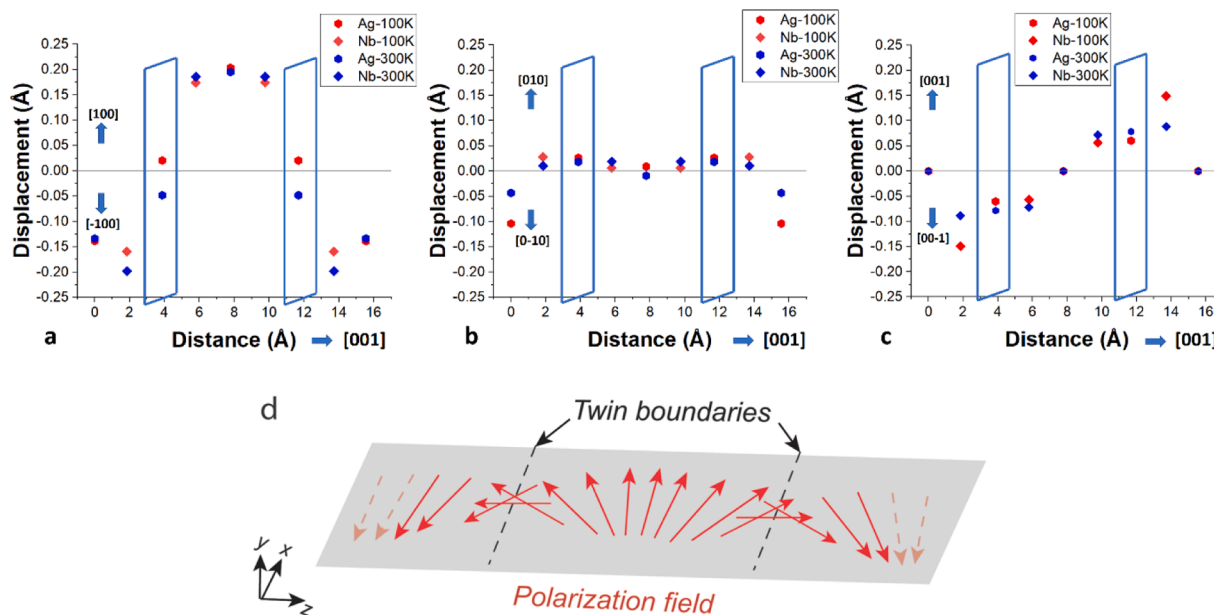
Fig. 4. Non-Ising ferroic domain boundaries in AGN at 100 K. **(a,b,c)** The displacements of Ag and Nb cations along (**a**) $\langle 100 \rangle$, (**b**) $\langle 010 \rangle$, and (**c**) $\langle 001 \rangle$ at their position along the ***c*** axis from the origin are shown. Blue rectangles show the 180° domain boundaries at $c = 0.25$ and 0.75. **(d)** Schematic illustration of the polarization field across mixed non-Ising twin boundaries, which is based on the experimentally measured cation displacements shown above. Note that the solid and the dotted lines indicate polarization directions with positive and negative y-components, respectively.

Table 1
Magnitude of net polarisation along [100], [010], and [001] calculated at 100 K and 300 K using the atomic coordinates observed from PDF refinement.

Temp (K)	Px ($\mu C/cm^2$)	Py ($\mu C/cm^2$)	Pz ($\mu C/cm^2$)
100K-Local	1.668	7.5E-15	2.1E-14
300K-Local	1.034	4.9E-15	3.2E-14

bond distance. In essence, variation in magnitude of the cation-centric dipoles partly arises from coupling between the nearby Nb-O and Ag-O bonds and its consequent influence on bond distances. In addition, tilting/rotation of the oxygen octahedra may further influence the net off-centering of the Ag atoms within the distorted O dodecahedra. Fig. 3 depicts the direction of tilting of the octahedra around the 110 axis and rotation of the octahedra around the 001 axis. For all the depicted Ag atoms, the surrounding oxygen octahedra exhibit out-of-phase tilting. However, for the $z = 0.5$ and $z = 0$ layers, the top and bottom octahedra are rotated in-phase around the 001 axis. In contrast, for the $z = 0.25$ (also $z = 0.75$) layer, the top and bottom octahedra are rotated out-of-phase around the 001 axis, which can play an important role in reducing the net Ag off-centering displacement and the resultant dipole moment for this layer (Layer 2 in Fig. 2b).

Earlier, in the context of AFE NaNbO$_3$, we proposed a structural model wherein the out-of-phase rotation across some octahedral layers is rationalized as a periodic stacking of a 180° twin variants [33,34]. Based on local structure analysis, we also showed that the 180° twinning is driven by a dominance of A-site centric distortion (caused by octahedral tilting/rotation) over B-site centric distortion (caused by zone center displacement of Nb), which is indicated by their respective distortion indices, viz. *D*: ~10.5 for AO$_{12}$ over ~5.5 for BO$_6$ in NaNbO$_3$ [34]. Here, we demonstrate that the $P2_1am$ ferrielectric structure of AgNbO$_3$ can also be described as a periodic assemblage of 180° twin boundaries with some unique aspects. Fig. 4 shows cation displacements along $\langle 100 \rangle$, $\langle 010 \rangle$, and $\langle 001 \rangle$ at 100 K and 300 K, depicted as function of their respective positions along [001] axis. Since the dominant $\langle 100 \rangle$ component of the cation displacements flip by 180° near $c = 0.25$ and 0.75 (Fig 4a), the *ab* planes at $c = 0.25$ and 0.75 are defined as the twin boundaries. Importantly, although the $\langle 100 \rangle$ component dominates,

significant $\langle 010 \rangle$ and $\langle 001 \rangle$ components of cation displacements are also present (Fig 4b,c). The polarization along the three different crystal axes due to these atomic displacements are listed in the Table 1 (see Supplementary Information [36] for details of calculation) The non-zero $\langle 010 \rangle$ and $\langle 001 \rangle$ polarization components points out the unique non-Ising nature of the 180° twin boundaries in AgNbO$_3$ [35]. The cation displacements along $\langle 001 \rangle$, that is polarization vectors perpendicular to the depicted twin boundaries at $c = 0.25$ and 0.75, underlies the partial Neel-type characteristic of the twin boundaries. There is also a small polarization component along $\langle 010 \rangle$, which indicates some degree of Bloch-type characteristic. Essentially, the $P2_1am$ structural model in AgNbO$_3$ encapsulates a non-Ising character of the periodic 180° twin boundaries, a schematic view of which is provided in Fig. 4d. Traditionally, 180° ferroic boundaries are described to have an Ising nature in which one principal polarization component flips by 180° across an interface and only changes allowed are for the magnitude of the polarization vector [44,45]. However, later studies indicated that ferroelectric domain boundaries can indeed have mixed Ising-Bloch-Neel characteristics, even in well-known ferroelectrics, such as BaTiO$_3$ and LiNbO$_3$ [46,47]. The non-Ising nature of a ferroic boundary can especially arise in the presence of multiple order parameters, in contrast to a single order parameter for Ising-like boundaries [35]. The two different structural prototypes for AFE (such as NaNbO$_3$) and ferrielectrics (such as AgNbO$_3$) can be understood in this context.

For AgNbO$_3$, the average *D* for AO$_{12}$ is 7.7, while average *D* for BO$_6$ is 5 (see Supplementary Information for details of calculation of *D* [36]). In comparison, for NaNbO$_3$, the *D* for AO$_{12}$ is 11, while the *D* for BO$_6$ is 5 [34]. That is, even though distortion around the A-site is larger than that around the B-site, the difference between them is lower in AgNbO$_3$ as compared to that in NaNbO$_3$. Since in NaNbO$_3$, the twin boundary is overwhelmingly influenced by A-site distortions, the A-site centric dipoles constitutes the primary order parameter and hence Ising-type twin boundaries can well describe the AFE structure of NaNbO$_3$. However, in AgNbO$_3$, the more comparable values of *D* for A- and B-sites ensures that both A- and B-site centric dipoles constitute multiple order parameters, thereby giving rise to non-Ising characteristic for the twin boundaries. In other words, the ferrielectric order as observed in AgNbO$_3$ is an intermediate state between antiferroelectric and ferroelectric states, whereby
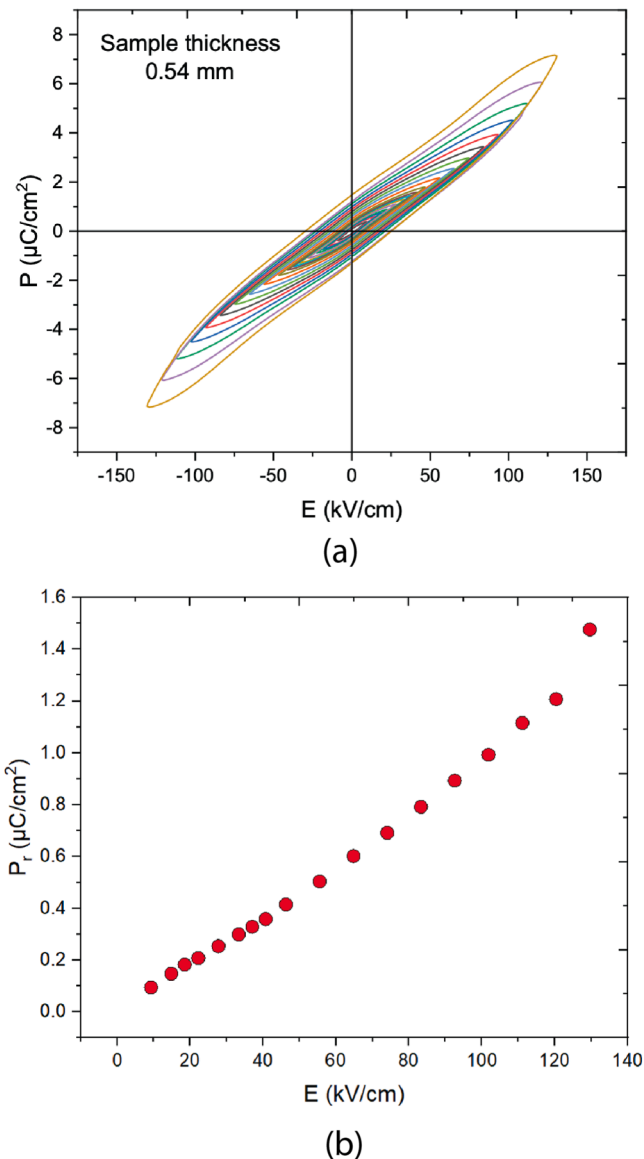
Fig. 5. (a) Polarization-electric field behavior, and (b) field-dependent variation in remanent polarization P_r of AgNbO$_3$ ceramics at low fields.

even though $D_{\text{A-site}} > D_{\text{B-site}}$, both order parameters constituting A-and B-site centric distortions have comparable influences on the nature of the periodic twin boundaries.

The atomistic structural model presented here is significant to understand the low-field polarization behavior of ferrielectric AgNbO$_3$, which is shown in (Fig. 5(a)). For electric-fields below the threshold field for ferrielectric-ferroelectric transition, $E_F \sim 150$ kV/cm [2], the material is supposed to be in the ferrielectric state. However, as shown in Fig. 5(b), the remanent polarization P_r increases with E, which discounts against a purely ferrielectric phase, since for a ferrielectric state the remanent polarization is not expected to increase with increase in electric-field amplitude. Instead, we propose that the observed non-linear increase in P_r below E_F is due to non-reversible 180° twin boundary motion.

In conclusion, we present evidence that indicates that the ferrielectric phase in AgNbO$_3$ is a periodic assemblage of 180° twin boundaries of non-Ising type, whose exact nature is determined by a delicate balance between local distortions around the A- and B-sites of the perovskite structure. Our atomistic model can describe the gradual transition from the FIE state to the AFE state with temperature and the

FIE state to the FE state with the application of an electric field. This insight provide useful guidance for the design of materials with mixed antiferroelectric/ferrielectric properties.

CRediT authorship contribution statement

T. Pramanik: Writing – review & editing, Writing – original draft, Methodology, Investigation, Formal analysis, Data curation, Conceptualization. **Cho Sandar Htet:** Writing – review & editing, Investigation, Formal analysis, Data curation. **Alicia Manjón-Sanz:** Writing – review & editing, Investigation, Formal analysis, Data curation. **J. Liu:** Validation, Investigation, Data curation. **S. Ullah:** Writing – review & editing, Data curation. **J. Kong:** Writing – review & editing, Formal analysis, Data curation. **C. Babori:** Writing – review & editing, Investigation, Data curation. **A. Brézard-Oudot:** Writing – review & editing, Investigation, Data curation. **L. Daniel:** Writing – review & editing, Data curation. **S.T. Misture:** Writing – review & editing, Investigation, Formal analysis, Data curation. **A. Pramanick:** Writing – review & editing, Supervision, Project administration, Investigation, Funding acquisition, Conceptualization.

Declaration of competing interest

The authors declare that they have no known competing financial interests or personal relationships that could have appeared to influence the work reported in this paper.

Supplementary materials

Supplementary material associated with this article can be found, in the online version, at doi:10.1016/j.scriptamat.2024.116426.

References

[1] C.A. Randall, Z. Fan, I. Reaney, L.-Q. Chen, S. Trolier-McKinstry, Antiferroelectrics: history, fundamentals, crystal chemistry, crystal structures, size effects, and applications, J. Am. Ceram. Soc. 104 (2021) 3775–3810.
[2] Z. Lu, W. Bao, G. Wang, et al., Mechanism of enhanced energy storage density in AgNbO3 -based lead-free antiferroelectrics, Nano Energy 79 (2021) 105423.
[3] Z. Liu, J. Lu, Y. Mao, P. Ren, H. Fan, Energy storage properties of NaNbO3-CaZrO3 ceramics with coexistence of ferroelectric and antiferroelectric phases, J. Eur. Ceram. Soc. 38 (2018) 4939–4945.
[4] N. Novak, F. Weyland, S. Patel, H. Guo, X. Tan, J. Rödel, J. Koruza, Interplay of conventional with inverse electrocaloric response in (Pb,Nb)(Zr,Sn,Ti)O3 antiferroelectric materials, Phys. Rev. B 97 (2018) 094113.
[5] C. Kittel, Theory of antiferroelectric crystals, Phys. Rev. 82 (5) (1951) 729.
[6] G. Shirane, E. Sawaguchi, Y. Takagi, Dielectric properties of lead zirconate, Phys. Rev. 84 (3) (1951) 476.
[7] X. Tan, et al., Can an electric field induce an antiferroelectric phase out of a ferroelectric phase? Phys. Rev. Lett. 105 (25) (2010) 255702.
[8] X. Tan, et al., The antiferroelectric↔ ferroelectric phase transition in lead-containing and lead-free perovskite ceramics, J. Am. Ceramic Soc. 94 (12) (2011) 4091–4107.
[9] B. Mani, et al., Critical thickness for antiferroelectricity in PbZrO 3, Phys. Rev. Lett. 115 (9) (2015) 097601.
[10] T. Ma, et al., Uncompensated polarization in incommensurate modulations of perovskite antiferroelectrics, Phys. Rev. Lett. 123 (21) (2019) 217602.
[11] Z. Fu, et al., Unveiling the ferrielectric nature of PbZrO3-based antiferroelectric materials, Nat. Commun 11 (1) (2020) 3809.
[12] Y. Yao, et al., Ferrielectricity in the archetypal antiferroelectric, PbZrO3, Adv. Mater. 35 (3) (2023) 2206541.
[13] P. Dufour, T. Maroutian, M. Vallet, et al., Ferroelectric phase transitions in epitaxial antiferroelectric PbZrO₃ thin films, App. Phys. Rev. 10 (2023) 021405.
[14] Y. Liu, R. Niu, A. Majchrowski, et al., Translational boundaries as incipient ferrielectric domains in antiferroelectric PbZrO3, Phys. Rev. Lett. 130 (2023) 216801.

[15] H. Ding, S. Egert, B. Huang, et al., Probing cation displacements in antiferroelectrics: a joint NMR and TEM approach, Chem. Mater. 35 (2023) 10041–10049.

[16] D. Fu, et al., AgNbO3: a lead-free material with large polarization and electromechanical response, Appl. Phys. Let.t 90 (25) (2007).

[17] L. Zhao, et al., Lead-free antiferroelectric silver niobate tantalate with high energy storage performance, Adv. Mater. 29 (31) (2017) 1701824.

[18] N. Luo, et al., Constructing phase boundary in AgNbO3 antiferroelectrics: pathway simultaneously achieving high energy density and efficiency, Nat Commun 11 (1) (2020) 4824.

[19] M. Francombe, B. Lewis, Structural and electrical properties of silver niobate and silver tantalate, Acta. Crystallogr. 11 (3) (1958) 175–178.

[20] A. Kania, K. Roleder, M. Łukaszewski, The ferroelectric phase in AgNbO3, Ferroelectrics 52 (1) (1983) 265–269.

[21] A. Kania, S. Miga, Preparation and dielectric properties of Ag1− xLixNbO3 (ALN) solid solutions ceramics, Mater. Sci. Eng. 86 (2) (2001) 128–133.

[22] A. Saito, et al., Growth of lithium doped silver niobate single crystals and their piezoelectric properties, Mater. Sci. Eng. 120 (1–3) (2005) 166–169.

[23] J. Fábry, et al., Silver niobium trioxide, AgNbO3, Acta. Crystallograph. Section C 56 (8) (2000) 916–918.

[24] P. Sciau, et al., Structural investigation of AgNbO3 phases using x-ray and neutron diffraction, J. Phys. 16 (16) (2004) 2795.

[25] I. Levin, et al., Structural changes underlying the diffuse dielectric response in AgNbO 3, Phys. Rev. B 79 (10) (2009) 104113.

[26] G. Li, et al., Atomic-scale structure characteristics of antiferroelectric silver niobate, Appl. Phys. Lett 113 (24) (2018).

[27] M. Yashima, et al., Structure of ferroelectric silver niobate AgNbO3, Chem. Mater. 23 (7) (2011) 1643–1645.

[28] T. Zhang, et al., Low-Temperature Phase Transition in AgNbO 3, J. Am. Ceramic Soc. 97 (6) (2014) 1895–1898.

[29] Y. Tian, et al., Ferroelectric transitions in silver niobate ceramics, J. Mater. Chem. C 7 (4) (2019) 1028–1034.

[30] U. Farid, A.S. Gibbs, B.J. Kennedy, Impact of li doping on the structure and phase stability in agnbo3, Inorg. Chem 59 (17) (2020) 12595–12607.

[31] J. Gao, et al., Lead-free antiferroelectric AgNbO3: phase transitions and structure engineering for dielectric energy storage applications, J. Appl. Phys. 128 (7) (2020).

[32] J. Gao, et al., Local atomic configuration in pristine and A-site doped silver niobate perovskite antiferroelectrics, Research (2022).

[33] C.S. Htet, et al., Atomic structural mechanism for ferroelectric-antiferroelectric transformation in perovskite NaNbO 3, Physical Review B 105 (17) (2022) 174113.

[34] C.S. Htet, et al., Effect of local structural distortions on antiferroelectric–ferroelectric phase transition in dilute solid solutions of K x Na1−x NbO3, Inorg. Chem. 61 (50) (2022) 20277–20287.

[35] G. Nataf, et al., Domain-wall engineering and topological defects in ferroelectric and ferroelastic materials, Nat. Rev. Phys. 2 (11) (2020) 634–648.

[36] Supplementary Information.

[37] D.A. Keen, A.L. Goodwin, The crystallography of correlated disorder, Nature 521 (7552) (2015) 303–309.

[38] T. Egami, S.J. Billinge, Underneath the Bragg peaks: Structural Analysis of Complex Materials, Elsevier, 2003.

[39] D.A. Keen, Perovskites take the lead in local structure analysis, IUCrJ 3 (1) (2016) 8–9.

[40] Varley F. Sears, Neutron scattering lengths and cross-sections, Neutr. News 3 (3) (1992).

[41] T. Egami, Local structure of ferroelectric materials, Annu. Rev. Mater. Res. 37 (2007) 297–315.

[42] T. Zhang, C. Zhang, L. Wang, Y. Chai, S. Shen, Y. Sun, H. Yuan, S. Feng, Low-temperature phase transition in AgNbO₃, J. Am. Ceram. Soc. 97 (2014) 1895–1898.

[43] R.E. Cohen, Origin of ferroelectricity in perovskite oxides, Nature 358 (1992) 136–138.

[44] V.L. Ginzburg, Several remarks on second-order phase transitions and microscopic theory of ferroelectrics", *Fiz. Tverd. Tela* (Leningrad) 2 (1960) 2031 [*Sov. Phys. Solid State* 2 1824 (1961)].

[45] Y. Ishibashi, E.K.H. Salje, On the thickness of domain walls in ferroelectrics and ferroelastics, Phase Trans. 67 (1998) 363–372.

[46] X.R. Huang, X.B. Hu, S.S. Jiang, D. Feng, Theoretical model of 180 domain-wall structures and their transformation in ferroelectric perovskites, Phys. Rev. B 55 (1997) 5534–5537.

[47] D. Lee, R.K. Behera, P. Wu, H. Xu, Y.L. Li, S.B. Sinnott, S.R. Phillpot, L.Q. Chen, V. Gopalan, Mixed Bloch-Néel-Ising character of 180 ferroelectric domain walls, Phys. Rev. B 80 (2009) 060102 (R).

Supplementary Information

An atomistic structural description of the ferrielectric polar phase involving non-coplanar cation displacements

T. Pramanik,[1] Cho Sandar Htet,[1] Alicia Manjón-Sanz,[2*] J. Liu,[2] S. Ullah,[1] J. Kong,[1] C. Babori,[3,4] A. Brézard-Oudot,[3] L. Daniel,[3,4] S. T. Misture,[5] A. Pramanick[6*]

[1] *Department of Materials Science and Engineering, City University of Hong Kong, Hong Kong, China*
[2] *Neutrons Scattering Division, Oak Ridge National Laboratory, Oak Ridge, Tennessee 37831, USA*
[3] *Group of Electrical and Electronic Engineers, Paris, University Paris-Saclay, Gif-sur-Yvette, France*
[4] *Sorbonne Université, CNRS, Laboratoire de Génie Electrique et Electronique de Paris, 75252 Paris, France*
[5] *Kazuo Inamori School of Engineering, Alfred University, Alfred, New York 14802, USA*
[*]manjonsanzam@ornl.gov, [*]abhijit.pramanick@centralesupelec.fr

I. Experimental details

A. Material Preparation:

AgNbO$_3$ ceramic samples were prepared using conventional solid-state reaction method with sintering under flowing oxygen. Stoichiometric amounts of Ag$_2$O (99.99%, Sigma Aldrich) and Nb$_2$O$_5$ (99.99%, Sigma Aldrich) powders were ball-milled in ethanol for 24 h using a planetary ball mill. After drying, the mixtures were calcined at 950° C for 8 h, using a tube furnace, in flowing oxygen at a rate of 500 cm^3 min^{-1}. The calcined powders were milled in ethanol for 12 hours. After drying, the powders were mixed with 5 wt% polyvinyl alcohol (PVA) solution and then pressed into pellets with a diameter of 12 mm and 1.5 mm thickness under 400 MPa pressure. The pellets were heated at a rate of 5° C min^{-1} to 600° C and held at this temperature for two hours to burn off the PVA. The samples were subsequently sintered at temperatures 1000° C in oxygen at a flow rate of 500 cm^3 min^{-1} for 8 h, then cooled to ambient temperature at a rate of 5° C min^{-1}. The AgNbO$_3$ pellets were ground using an agate mortar and pestle and sieved through a 200-μm mesh for neutron diffraction and scattering experiments. During sintering, the pellets were covered with calcinated AgNbO$_3$ powders to mitigate the volatilization of metal atoms.

The following figure shows representative scanning electron micrographs of fracture surface of sintered AGN ceramics. The fracture surface revealed dense microstructure with minimal porosity. Magnified view from selected region indicates that the grain sizes are in the range of few microns.
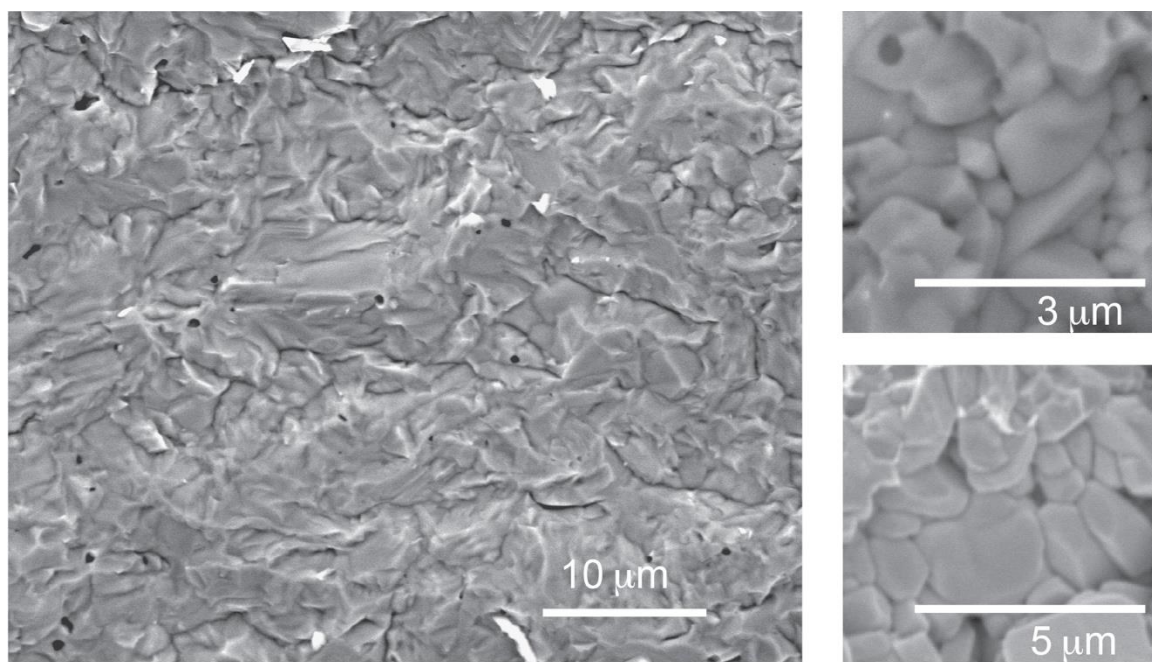
Figure S1: Scanning electron micrographs of fracture surface of AgNbO$_3$ ceramics. Large area micrograph on the left shows dense pore-free microstructure. High magnification images from selected areas on the right indicates grain sizes of a few microns.

B. Experimental Measurements:

Ambient temperature X-ray powder diffraction (XRD) was performed using a Bruker D-8 diffractometer with Lynxeye XE position-sensitive detector, while in-situ high temperature studies were performed on a Bruker D-8 with samples loaded as a packed powder in an Anton-Paar HTK1200 diffraction furnace. The diffractometer was equipped with a Bruker Vantec linear position-sensitive detector to enable rapid XRD pattern acquisition over the angular range of 20 to 120 °2Θ. The XRD system was calibrated using NIST SRM660a LaB6 powder in order to determine the instrument response up to 120 °2Θ and the Rietveld analysis was performed using GSAS-II [S1].

Time-of-flight neutron-scattering measurements were conducted at the Spallation Neutron Source (Oak Ridge National Laboratory). Neutron-diffraction (ND) experiments were performed at the POWGEN instrument [S2]. Approximately, 3 g of $AgNbO_3$ powder sample was sealed in a 6-mm-diameter vanadium can with helium exchange gas and loaded in the POWGEN automatic changer. At first, the sample was cooled down to 100K for data collection and then heated to 300K for room temperature data collection with a heating rate of 5 K/min. Total neutron-scattering measurements were conducted at the NOMAD instrument using Automated Sample Changer with Cobra Cryostream [S3]. The measured scattering intensities were normalized against proton charge and scattering from a 6-mm vanadium rod to correct for neutron flux and detector efficiency. The total scattering data cutoff at a maximum wavevector transfer Q_{max} of 45 Å^{-1} was used for the Fourier transform to the reduced pair distribution function, which is defined by the following function:

$$G(r) = \left(\frac{2}{\pi}\right) \int_{Q_{min}}^{Q_{max}} Q(S(Q)-1)\sin(Qr)dQ, (1)$$

where G(r) is related to the atom-pair density function $\rho(r)$ and the pair distribution function g(r) through the following relations:

$$G(r) = 4\pi r \left[\rho(r) - \rho_0\right] = 4\pi r \rho_0 \left[g(r)-1\right], (2)$$

where ρ_0 is the atomic number density.[S4,S5] Small-box modeling of the PDF data was conducted with PDFgui packages [S4].

II. Results

A: Rietveld refinement of diffraction patterns:
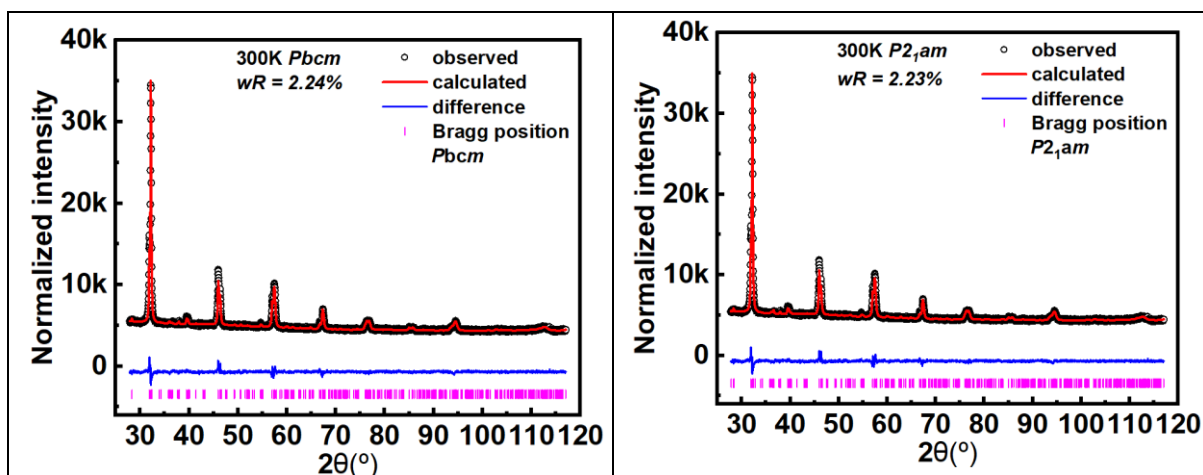
Figure S2: Rietveld refinement of AgNbO3 using X-ray diffraction data measured at 300K with (a) *P*2₁*ma* space group, and (b) *Pbcm* space group. Observed (black symbol), calculated (red line), difference (blue line) profiles, and Bragg positions (pink ticks) obtained after the Rietveld refinement using GSAS II software. Weighted residuals (Rw) are shown for all the refinements.
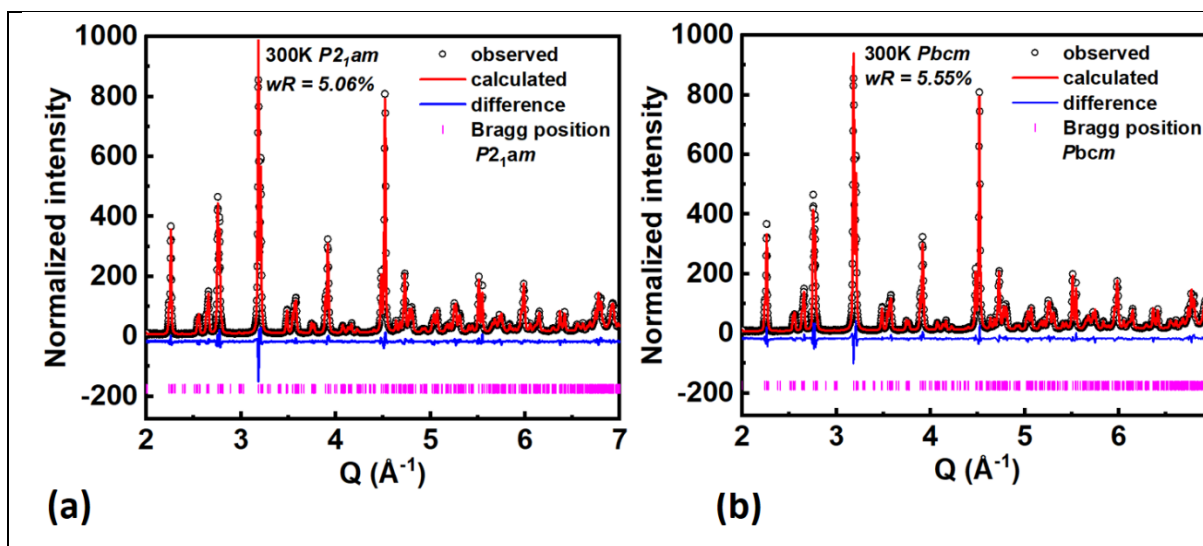
Figure S3: Rietveld refinement of AgNbO3 using neutron diffraction data measured at 300K with (a) *P*2₁*ma* space group, and (b) *Pbcm* space group. Observed (black symbol), calculated (red line), difference (blue line) profiles, and Bragg positions (pink ticks) obtained after the Rietveld refinement using GSAS II software. Weighted residuals (Rw) are shown for all the refinements.

B. Box-car refinement of G(r)

Box-car type refinements over different r-ranges were performed in order to estimate the length-scale of the local polar $P2_1am$ structure. The results are shown below. It is clearly seen that the residual R_w increases steeply beyond $r \sim 24$ Å, which indicates that beyond this length-scale the structure averages out to a non-polar $Pbcm$ structure.
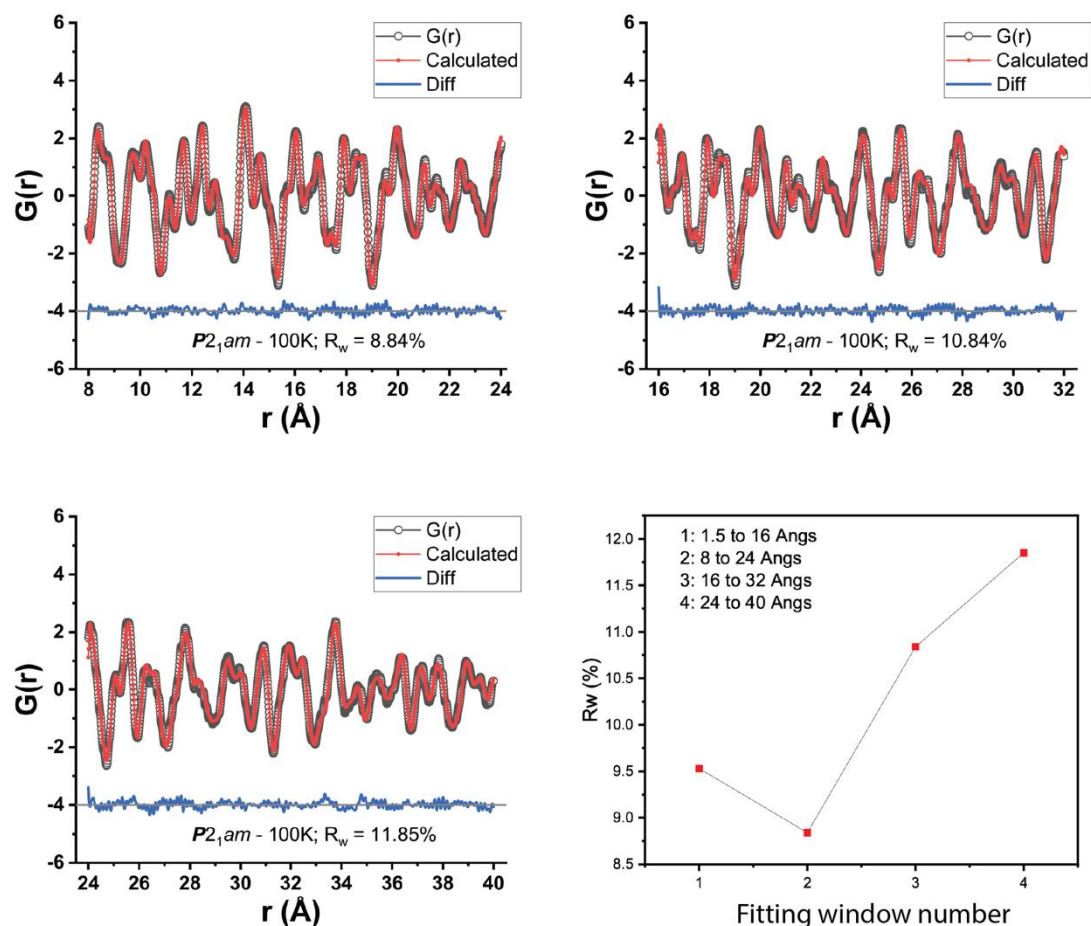
Figure S4: Fitting of neutron G(r) over different r-ranges. The respective R_w values for each fitting window are shown at the bottom.

C. Polarization Calculation:

Calculation of P_x using 100 K local atomic coordinates observed from PDF refinement.

Atom name	x	x normal	dx	Q (**C**)	Q.dx (**C.m**)
Ag1	0.748799	0.75	-6.73006E-13	1	-1.07681E-31
Ag2	0.248799	0.25	-6.73006E-13	1	-1.07681E-31
Ag3	0.248799	0.25	-6.73006E-13	1	-1.07681E-31
Ag4	0.748799	0.75	-6.73006E-13	1	-1.07681E-31
Ag5	0.772876	0.75	1.2819E-11	1	2.05105E-30
Ag6	0.272876	0.25	1.2819E-11	1	2.05105E-30
Ag7	0.721231	0.75	-1.61213E-11	1	-2.57941E-30

Ag8	0.221231	0.25	-1.61213E-11	1	-2.57941E-30
Nb1	0.271398	0.25	1.19908E-11	5	9.59265E-30
Nb2	0.771398	0.75	1.19908E-11	5	9.59265E-30
Nb3	0.771398	0.75	1.19908E-11	5	9.59265E-30
Nb4	0.271398	0.25	1.19908E-11	5	9.59265E-30
Nb5	0.717623	0.75	-1.81431E-11	5	-1.45145E-29
Nb6	0.217623	0.25	-1.81431E-11	5	-1.45145E-29
Nb7	0.217623	0.25	-1.81431E-11	5	-1.45145E-29
Nb8	0.717623	0.75	-1.81431E-11	5	-1.45145E-29
O1	0.257982	0.25	4.47288E-12	-2	-1.43132E-30
O2	0.757982	0.75	4.47288E-12	-2	-1.43132E-30
O3	0.757982	0.75	4.47288E-12	-2	-1.43132E-30
O4	0.257982	0.25	4.47288E-12	-2	-1.43132E-30
O5	0.235365	0.25	-8.20103E-12	-2	2.62433E-30
O6	0.735365	0.75	-8.20103E-12	-2	2.62433E-30
O7	0.522059	0.5	1.23612E-11	-2	-3.95559E-30
O8	0.022059	0	1.23612E-11	-2	-3.95559E-30
O9	0.022059	0	1.23612E-11	-2	-3.95559E-30
O10	0.522059	0.5	1.23612E-11	-2	-3.95559E-30
O11	0.45225	0.5	-2.67577E-11	-2	8.56247E-30
O12	0.95225	1	-2.67577E-11	-2	8.56247E-30
O13	0.95225	1	-2.67577E-11	-2	8.56247E-30
O14	0.45225	0.5	-2.67577E-11	-2	8.56247E-30
O15	0.757314	0.75	4.09855E-12	-2	-1.31154E-30
O16	0.257314	0.25	4.09855E-12	-2	-1.31154E-30
O17	0.020433	0	1.14501E-11	-2	-3.66402E-30
O18	0.520433	0.5	1.14501E-11	-2	-3.66402E-30
O19	0.520433	0.5	1.14501E-11	-2	-3.66402E-30
O20	0.020433	0	1.14501E-11	-2	-3.66402E-30
O21	0.46017	0.5	-2.23196E-11	-2	7.14226E-30
O22	0.96017	1	-2.23196E-11	-2	7.14226E-30
O23	0.96017	1	-2.23196E-11	-2	7.14226E-30
O24	0.46017	0.5	-2.23196E-11	-2	7.14226E-30
				Dipole moment	**8.06594E-30 C.m**
				Px	**0.016676347 C/m^2**

D. Distortion parameter calculation:

The magnitude of the octahedral and cubooctahderal distortions (*D*) can be calculated according to the equation

$$D = \frac{1}{n}\left[\sum_{i}^{n} \frac{|d_i - d|}{d} \right] \qquad (3)$$

where n is the coordination number d_i and d are the individuals and average values of the different A(B) – O interatomic distances, respectively [S6].

For the AGN structure, D was calculated for the different Ag and Nb sites. In case of presence of two crystallographic phases, the relative fraction of each ratio was taken into account to calculate the average value of D for a particular crystallographic site.
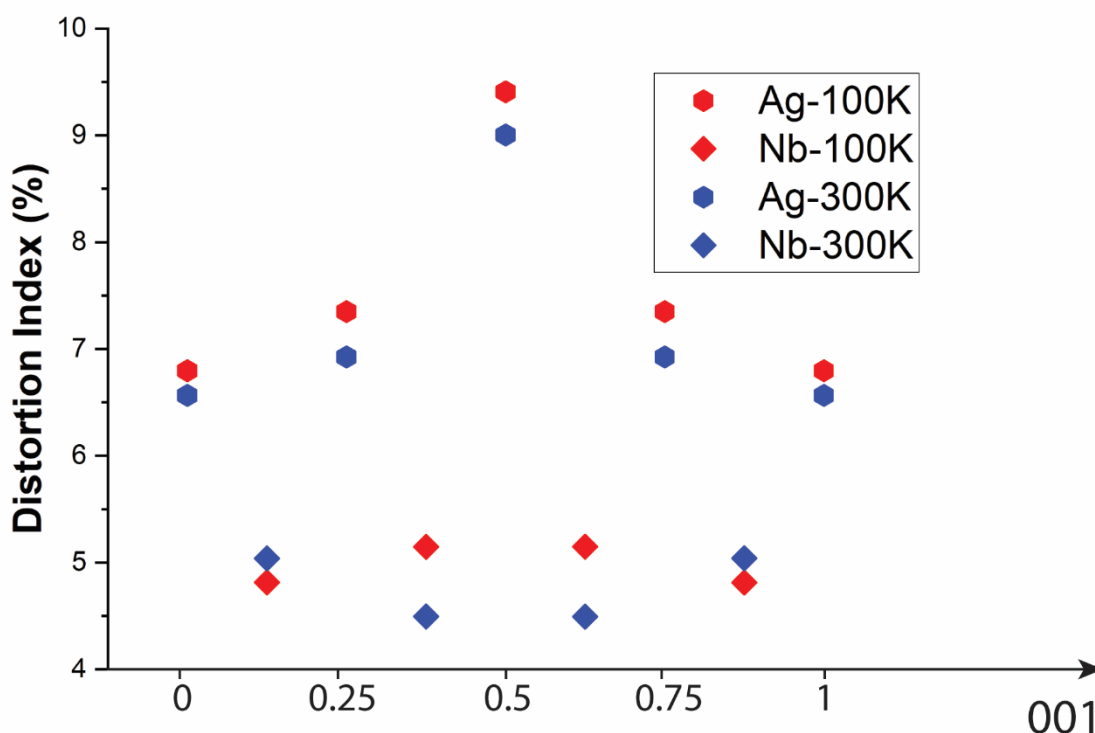
Figure S5: Calculated values of D for various Ag and Nb sites, which are plotted as a function of their relative position along the 001 crystallographic axis.

References:

S1. Toby, B. H., and Von Dreele, R. B. (**2013**). "GSAS-II: The Genesis of a Modern Open-Source All-Purpose Crystallography Software Package," Journal of Applied Crystallography **46**, 544-549. doi:10.1107/S0021889813003531

S2. Huq, A., et al., *POWGEN: rebuild of a third-generation powder diffractometer at the Spallation Neutron Source.* Journal of Applied Crystallography, 2019. **52**(5): p. 1189-1201.

S3. Neuefeind, J., et al., *The nanoscale ordered materials diffractometer NOMAD at the spallation neutron source SNS.* Nuclear Instruments and Methods in Physics Research Section B: Beam Interactions with Materials and Atoms, 2012. **287**: p. 68-75.

S4. Farrow, C., et al., *PDFfit2 and PDFgui: computer programs for studying nanostructure in crystals.* Journal of Physics: Condensed Matter, 2007. **19**(33): p. 335219.

S5.   Keen, D. A. A comparison of various commonly used correlation functions for describing total scattering. J. Appl. Crystallogr. **2001**, 34, 172-177.

S6.   Kong, J.; Li, L.; Liu, J.; Marlton, F.; Jorgensen, M. R. V.; Pramanick, A. A local atomic mechanism for monoclinic-tetragonal phase boundary creation in Li-doped Na0.5K0.5NbO3 ferroelectric solid-solution. Inorg. Chem. 61, (2022) 4335-4349.